nature communications

Article

https://doi.org/10.1038/s41467-026-71634-2

Probing resonances in the double-well entry valley of the Cl + NH_3 reaction using high-resolution anion photoelectron spectroscopy

Received: 5 October 2025

Accepted: 23 March 2026

Published online: 22 April 2026

Check for updates

Shuaiting Yan[1,2], Rui Zhang[1], Wenru Jie[1], Jiayi Chen[1], Mingjuan Yang[3], Hongwei Song[3] ✉ & Chuangang Ning[1] ✉

The Cl + NH_3 → HCl + NH_2 reaction is a prototypical system featuring multiple potential wells and transition states along the reaction pathway, presenting significant challenges for achieving a fully quantum-state-resolved understanding of its dynamics. By photodetaching $ClNH_3^-$ anions, we probe the transition-state region in the reaction using high-resolution photoelectron spectroscopy combined with exact quantum dynamics calculations. Two prominent electronic bands are observed experimentally. High-level multi-reference calculations indicate that they arise from chlorine atom spin–orbit coupling. Several Feshbach resonances are identified in the lower spin–orbit state and assigned by excitations of the N–Cl translational, NH_3 umbrella, and NH_3–Cl rocking modes of the pre-reaction complexes RC1 and RC2. Impressively, a Walden inversion-like transformation between RC1 and RC2 is identified, driven by NH_3 hydrogen reorientation via the umbrella mode excitation. These findings reveal that transition-state spectroscopy offers unprecedented opportunities to deepen our physical understanding of polyatomic reactions by probing their intricate mechanisms.

Understanding elementary chemical reactions at a fully quantum-state-resolved level is crucial in fundamental chemistry research, which not only deepens our understanding of microscopic processes of chemical reactions but also reveals how quantum effects influence these reactions. The combination of sophisticated crossed molecular beam experiments and high-level theoretical calculations has provided major insights into how the fundamental interactions govern reaction dynamics[1–4]. Furthermore, Zewail et al. pioneered pump-probe experimental techniques to monitor reaction dynamics in real time[5–7]. Meanwhile, time-resolved cavity-enhanced direct frequency comb spectroscopy has been employed to clarify the formation mechanism and quantify the yield of the HOCO intermediate in the OH + CO reaction[8]. In this regard, negative ion photoelectron spectroscopy provides complementary insights through direct probe of the transition-state region via photodetachment of an anion geometrically similar to the neutral transition state[9–16]. A representative study by Neumark et al. employed an integrated approach of high-resolution image-based spectroscopy and quantum dynamics calculations to elucidate the neutral vinylidene-acetylene isomerization kinetic process[17]. Transition-state spectroscopy utilizing photodetachment of negative ions has been proven to be a powerful method for interrogating topologies of reactive potential energy surfaces, as

[1]Department of Physics, State Key Laboratory of Low Dimensional Quantum Physics, Frontier Science Center for Quantum Information, Tsinghua University, Beijing, China. [2]National Key Laboratory of Science and Technology on Advanced Light-Duty Gas-Turbine, Institute of Engineering Thermophysics, Chinese Academy of Sciences, Beijing, China. [3]State Key Laboratory of Magnetic Resonance Spectroscopy and Imaging, Innovation Academy for Precision Measurement Science and Technology, Chinese Academy of Sciences, Wuhan, China. ✉e-mail: hwsong@wipm.ac.cn; ningcg@tsinghua.edu.cn

https://doi.org/10.1038/s41467-026-71634-2

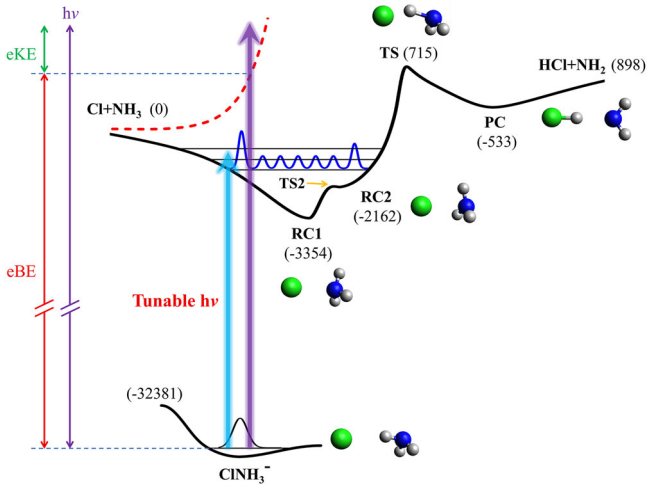

Fig. 1 | Energy diagram for photodetachment of the $ClNH_3^-$ anion to the neutral $Cl + NH_3 \rightarrow HCl + NH_2$ reaction. The upper red dashed curve depicts the neutral potential energy surface (PES) of the spin–orbit coupling (SOC) excited state. The upper bold curve is the neutral reaction minimum energy path (MEP) that connects the reactants and products. The lower thick curve depicts the anion potential energy surface. Structures are shown for the reactant complexes (RC1 and RC2), transition state (TS), product complex (PC) and anion using gray (H), blue (N) and green (Cl). Energies of stationary points are shown in parentheses (in cm^{-1}) relative to the reactant asymptote with zero-point energy corrected. The relationship between the photon energy ($h\nu$), electron binding energy (eBE) and electron kinetic energy (eKE) in the cryo-SEVI experiment is also indicated.

demonstrated for $F + H_2$[18,19], $Cl + H_2/D_2$[20], $F + CH_4$[21,22], $F + NH_3$[23,24], $F + CH_3OH$[25], $F + H_2O$[26,27].

The gas-phase reaction $Cl + NH_3 \rightarrow HCl + NH_2$ is a prototypical hydrogen-abstraction reaction[28]. This reaction has garnered significant experimental and theoretical interest over recent decades, focusing primarily on its kinetics[29–35]. High-level theoretical calculations have identified several intermediate complexes along its minimum energy path (MEP), which have been proved to have visible effect on its dynamics. Actually, the attractive interactions between reactants have been found to play a critical role in directing the reaction pathway and dynamics in many chemical reactions[36–44]. Monge-Palacios et al. carried out quasi-classical trajectory (QCT) and reduced-dimensional quantum mechanical (QM) calculations on an analytical potential energy surface (PES) to investigate the reactivity and mechanism of the reaction[45,46]. Recently, Tu et al. built a globally accurate, full-dimensional, and spin–orbit-corrected PES for the reaction[47]. The calculated thermal rate constants on the ab initio-based PES agreed well with experimental values. Meanwhile, Chen et al. explored the typical multichannel $H + NH_2Cl$ reaction and predicted a novel reaction mechanism termed "heavy-atom assisted rotation" via high-level ab initio calculations[48]. To our best knowledge, chlorine is the heaviest element studied to date using transition-state spectroscopy in a polyatomic reaction system. The theoretical description of Cl-containing polyatomic reaction systems using quantum chemical and dynamical methods remains particularly challenging. Our present work aims to provide reliable experimental benchmarks for this endeavor through transition-state spectroscopy of the $Cl + NH_3 \rightarrow HCl + NH_2$ reaction.

In this work, we report a joint anion photoelectron spectroscopy and quantum dynamics study of the $Cl + NH_3 \rightarrow HCl + NH_2$ reaction. Two prominent electronic bands and several Feshbach resonances in the low-energy band are detected by photodetaching the $ClNH_3^-$ anion. A Walden inversion-like transformation between the pre-reaction complexes RC1 and RC2 is identified. These findings reveal that transition-state spectroscopy offers unique opportunities to deepen our physical understanding of polyatomic reactions dynamics.

Results

In the present work, we report a combined high-resolution photoelectron spectroscopy and quantum dynamics study of the $Cl + NH_3 \rightarrow HCl + NH_2$ hydrogen-abstraction reaction, based on photodetachment of the stable $ClNH_3^-$ anion. Spectra were acquired via slow photoelectron velocity-map imaging of cryogenically cooled anions (cryo-SEVI), achieving energy resolutions up to a few cm^{-1}[49–54]. Unlike the exothermic $F + NH_3 \rightarrow HF + NH_2$ reaction[23,24], the $Cl + NH_3 \rightarrow HCl + NH_2$ reaction is an endothermic reaction. Figure 1 illustrates the probing of the transition-state region of the reaction through $ClNH_3^-$ photodetachment. The upper red dashed curve depicts the neutral potential energy surface (PES) of the spin–orbit coupling (SOC) excited state, which is a repulsive potential, meaning a dissociated state after photodetachment. The MEP connecting the reactants and products in their ground vibrational states is shown, together with the stationary-point energies and geometries. The neutral MEP features two van der Waals (vdW) wells (RC1 and RC2) in the entrance channel, a distinct transition state (TS), and a product complex (PC) well. The entrance valley vdW complexes lie at 3354 (RC1) and 2162 cm^{-1} (RC2) below the reactant asymptote, and a saddle point 715 cm^{-1} above the reactants. A shallow potential barrier (TS2) between the RC1 and RC2 enables facile interconversion of RC1 and RC2. Based on the theoretical assignments (Supplementary Table 3), the experimental spectra are demonstrated to contain features attributable to both RC1 and RC2. For the complex RC1, the three hydrogen atoms bonded to the nitrogen atom are located on the side away from the chlorine atom. In contrast, the three hydrogen atoms are deflected to the side closer to the chlorine atom when RC1 transforms into RC2. This structural transformation constitutes a Walden inversion-like process in the nucleophilic substitution (S_N2) reaction[55].

The measured spectra of $ClNH_3^-$ are presented in Fig. 2. The orange curve shows the overview spectrum obtained with the photodetachment laser wavelength at 290 nm. High-resolution composited spectrum (black), acquired at various photon energies, reveals finer vibrational structure. The experimental spectrum contains two prominent electronic bands: the first band contains several sharp peaks labeled as *a*–*i*, whereas the second lacks sharp features. The ~1000 cm^{-1} energy separation between two bands agrees well with the calculated 926 cm^{-1} spin–orbit (SO) splitting of the neutral system at the anion stationary geometry, as presented in the Suppl. Note 3, and is comparable to the 882 cm^{-1} SO splitting between $Cl(^2P_{3/2})$ and $Cl^*(^2P_{1/2})$ atomic states[21,22,56]. Due to the perturbation induced by NH_3, the ^2P state of the chlorine atom splits into two doubly degenerate $^2P_{3/2}$ states and one doubly degenerate $^2P_{1/2}$ state. As shown in Supplementary Table 4, relative to the non-relativistic ground-state energy, the $^2P_{1/2}$ state is raised by 719 cm^{-1}, while the two $^2P_{3/2}$ states are lowered by 34 cm^{-1} and 207 cm^{-1}, respectively. The close agreement between the experimental band separation and the theoretical SO splitting indicates that the two observed bands correspond to distinct spin–orbit states.

Figure 3 shows the two-dimensional SO splitting corrected PES along the bond-forming coordinate (Cl–NH_3) and the bond-breaking coordinate (H–NH_2), with all other coordinates optimized on the non-relativistic ground-state PES. Clearly, the $^2P_{1/2}$ state is repulsive along the minimum energy path (MEP), which would yield a photoelectron spectrum without resolved vibrational structure. In contrast, the lower $^2P_{3/2}$ state is attractive in the entrance valley and is expected to produce a spectrum with well-resolved vibrational features. These theoretical predications align closely with the experimental observations. Furthermore, the upper $^2P_{3/2}$ state is also repulsive along the MEP, similar to the $^2P_{1/2}$ state, and would therefore contribute a broad spectral envelope. However, this band is not distinctly observed in the experiment due to the small energy separation (only 173 cm^{-1}) between

the two $^2P_{3/2}$ states at vertical excitation. As a result, the broad spectral signature from the upper $^2P_{3/2}$ state overlaps with the vibrationally resolved spectrum from the lower $^2P_{3/2}$ state. In other words, the first experimental band contains contributions from both $^2P_{3/2}$ states, with the upper state providing a broad background.

For comparison, the raw theoretical $ClNH_3^-$ photoelectron spectrum (purple), as shown in Fig. 2, was convolved with a Gaussian function with a full width at half maximum (FWHM) value of 150 cm^{-1} for the low-resolution simulation (blue), and 75 cm^{-1} for the high-resolution simulation (red). Theoretical spectra were uniformly redshifted by 90 cm^{-1} to align simulated peaks with the experimental features. The first band is assigned to the SOC ground state. The vertical photodetachment transition to this state yields a spectrum exhibiting resolved vibrational fine structure. The detailed structure of the first band is well reproduced by the full-dimensional quantum dynamics calculations on the ground electronic state neutral PES. The absence of the second band at 33,100 cm^{-1} in the theoretical photoelectron spectrum is attributed to the SOC excited state, whose repulsive nature leads to a continuum-like feature upon vertical photodetachment from the $ClNH_3^-$ anion, lacking discrete vibrational peaks. The well-resolved peaks (*a*–*i*) correspond to photodetachment transitions from the anion ground state to high-lying quasi-bound states around the neutral RC1 and RC2 regions. Experimental and theoretical peak positions, along with their assignments, are summarized in Supplementary Table 3. The reactant asymptote for the $Cl + NH_3 \rightarrow HCl + NH_2$ reaction lies at 32,381 cm^{-1}, while the transition-state barrier is located at 33,279 cm^{-1}. These are marked in Fig. 2 with gray and black arrows, respectively. Peaks *a*–*g* lie below the reactant asymptote, indicating that they are bounded in the reactant complex (RC) wells, whereas peaks *h* and *i* lie above the reactant asymptote and below the transition-state barrier, implying that they are Feshbach resonance states.

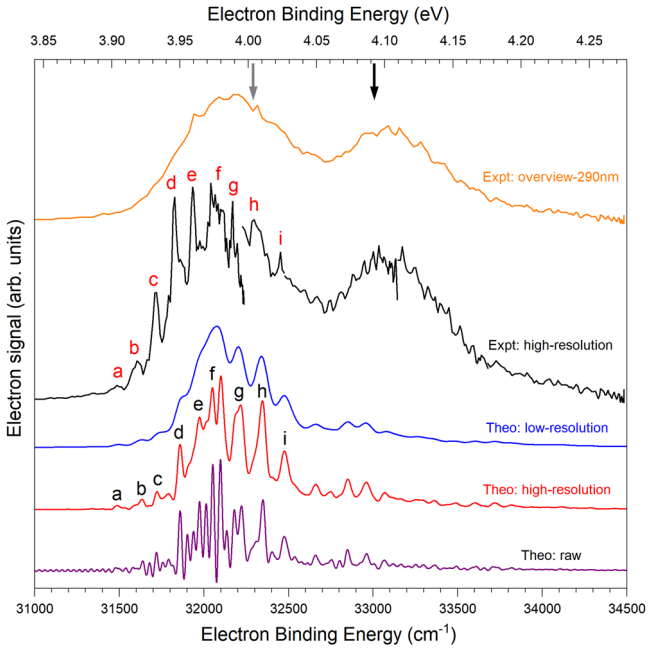

Fig. 2 | Experimental and theoretical photodetachment spectra of $ClNH_3^-$. The top spectrum (orange) is an experimental overview spectrum obtained at the laser wavelength 290 nm. Below it, the high-resolution spectrum is shown in black. Peaks in the first band are labeled as *a*–*i*. The second band lacks sharp features. The raw theoretical simulation (bottom, purple) is plotted with two convoluted spectra (blue with a 150 cm^{-1} FWHM Gaussian function and red with 75 cm^{-1}) for comparison. The gray arrow and the black arrow indicate the energy positions of the reactant asymptote and the transition-state, respectively.

Discussion

To better interpret the observed spectral features (*a*–*i*), vibrational wavefunctions corresponding to these peaks were calculated. As shown in Fig. 1, there exist two vdW wells in the entrance valley, which are separated by a shallow barrier (TS2). The excited states of both vdW complexes exhibit significant Franck-Condon overlaps with the anion ground state. Figure 4 displays the wavefunction density distribution $|\Psi(\phi_2)|^2$ along the NH_3–Cl azimuth angle ϕ_2 (defined in Supplementary Fig. 1) of the bound states assigned to spectral peaks *a*, *c*, *f*, and *i*. These distributions reveal that the photodetachment of the $ClNH_3^-$ anion creates a mixture of RC1 and RC2—not a single complex—demonstrating the approximate and dilemmatic nature of single-complex assignments. For example, the vibrational wavefunction of the specific bound state corresponding to peak *a* has a contribution of 57% from RC1 and 43% from RC2 if setting TS2 ($\phi_2 = 21.6°$) as the cut point. Similarly, the vibrational wavefunction of the specific bound state corresponding to peak *c* has a contribution of 36% from RC1 and 64% from RC2. The proportions of RC1 and RC2 for peaks *a*–*i* are listed in Supplementary Table 5. The changes in the proportions of the two components (RC1 and RC2) for different peaks imply that an isomer inversion occurs between RC1 and RC2 through a Walden inversion-like transformation.

Figure 5 displays two-dimensional (2D) cuts of several representative wavefunctions, superimposed on the neutral PES (the remaining wavefunctions are given in Supplementary Fig. 3). Unlike

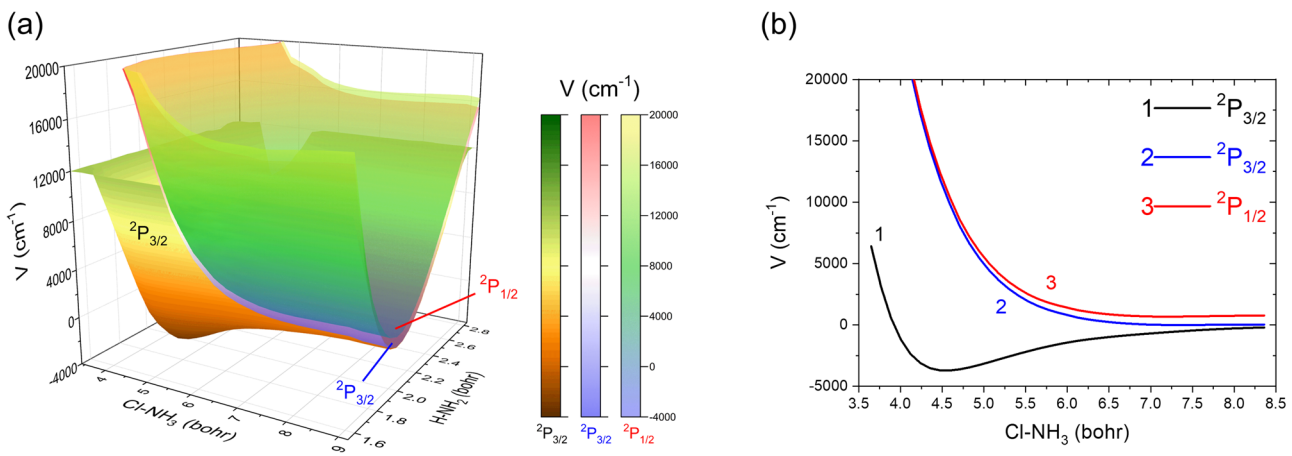

Fig. 3 | Spin–orbit splitting corrected potential energy surface (PES) of the $ClNH_3$complex. a The spin–orbit splitting PES along the bond-forming coordinate (Cl–NH_3) and the bond-breaking coordinate (H–NH_2). **b** The spin–orbit splitting curve along the minimum energy path (MEP) on the PES.

the H–F bond vibrational excitation observed in the $F + NH_3$ reaction[23,24], the H–Cl bond in the $Cl + NH_3$ reaction remains unexcited. To highlight this difference, 2D cuts of the wavefunctions are provided along the distances NH_3–Cl and N–H by fixing the remaining coordinates at the geometries of RC2 and RC1, respectively. The assignments of the vibrational wavefunctions were performed by analyzing their nodal patterns.

As shown in Fig. 5, the nodal count along the horizontal axis corresponds to the vibrational quantum number of the H_3N–Cl translational mode (υ_2). In the "Peak *a* RC2" panel, the wavefunction exhibits a single vibrational mode with six nodes, which is assigned as $\upsilon_2 = 6$. The anion ground-state wavefunction is also superimposed on the neutral PES contour to visualize their overlap during photodetachment. The anionic ground state shows a poor Franck-Condon overlap with the neutral vibrational ground state and low-lying state wavefunctions, explaining their absence in the spectra. Peak *c* is analogously assigned as $\upsilon_2 = 6$. In contrast, features *f*–*i* at higher energies exhibit delocalized wavefunctions, complicating the assignments. It can also be noted from Supplementary Fig. 4a, 4b that their wavefunctions span the entire angular space along θ_1, indicating that the complex becomes a free rotator at high energies.

The RC1 components exhibit higher vibrational nodes compared to RC2, indicating broader excitation dynamics. The assignment of peak *a* is $\upsilon_2 = 6$ for the RC2 component while it is $\upsilon_2 = 8$ for the RC1 component. The assignment of peak *c* is $\upsilon_2 = 6$ for the RC2 component and $\upsilon_2 = 4$ for the RC1 component. The excitation of the υ_2 mode is a result of the change in the N–Cl equilibrium distance. By examining the 2D cuts of the wavefunctions along the other coordinates (see in Supplementary Fig. 4a and Supplementary Fig. 4b), these quasi-bound states are formed by excitations in υ_3 and υ_6 as well. The υ_3 mode arises from the classical umbrella vibration of the ammonia molecule, exciting the Walden inversion between the RC1 and RC2. The υ_6 mode originates from the NH_3–Cl out-of-plane wagging motion. Photodetachment dynamics primarily involve these three vibrational modes of RC1/RC2. In addition, Supplementary Fig. 5 exhibits 2D cuts of the wavefunctions of peaks *a*–*i* along the distance NH_3–Cl and the azimuth angle ϕ_2, with the remaining coordinates fixed at the geometry of TS2. It can be seen that the wavefunctions are distributed on both sides of TS2, which accounts for the fact that the wavefunction of the specific bound state corresponding to each spectral peak exhibits features characteristic of both RC2 and RC1.

In conclusion, this study maps the transition-state region of the Cl + $NH_3 \rightarrow HCl + NH_2$ reaction through the combination of the high-resolution slow photoelectron velocity-map imaging spectroscopy and exact quantum dynamics calculations. Two prominent electronic bands are observed in the experimental photoelectron spectrum. These bands are identified, via high-level multi-reference calculations, as originating from chlorine atom spin–orbit coupling. The low-energy band exhibits a series of sharp peaks, which are accurately reproduced by quantum dynamics simulations. These peaks originate from the formed quasi-bound states in the reactant complex region of the neutral potential energy surface, unveiling a double-well entry valley in the reaction. The present results highlight the importance of pre-reactive van der Waals complexes for the Cl + $NH_3 \rightarrow HCl + NH_2$ reaction. The broad spectral envelope observed in the high-energy region arises from the repulsive upper spin–orbit state. The integrated methodology of cryo-SEVI spectroscopy and theoretical simulations establishes the anion photoelectron spectroscopy as a powerful tool for probing elusive reactive intermediates, and positions quantum

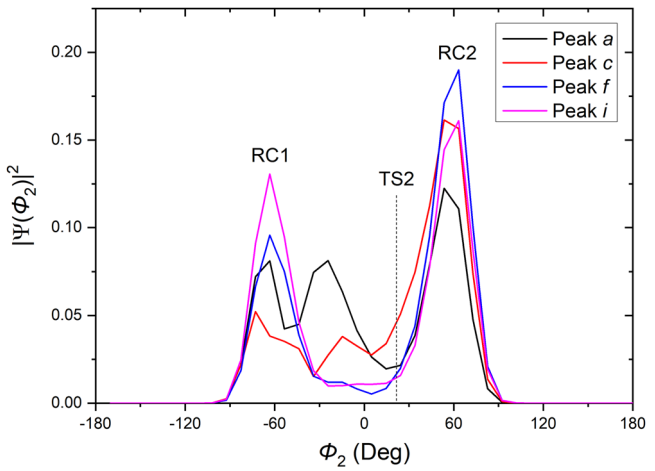

Fig. 4 | Density distribution of the wave function. The wavefunction density distribution ($|\Psi(\phi_2)|^2$) of spectral peaks *a*, *c*, *f*, and *i* along the azimuth angle ϕ_2.

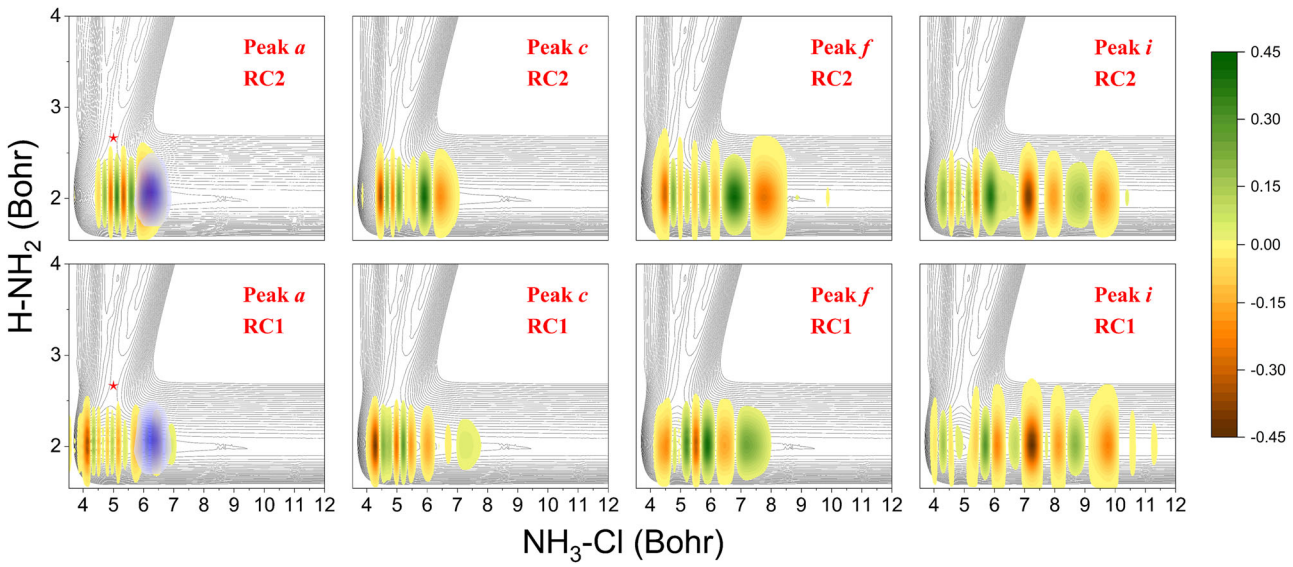

Fig. 5 | 2D cuts of the RC2 and RC1 vibrational wavefunctions accessed via photodetachment. The labels correspond to the observed peaks *a*, *c*, *f*, and *i* in Fig. 2. The wavefunctions are superimposed on the neutral PES, and the transition state is marked with a red star. The blue area in panels "Peak *a* RC2" and "Peak *a* RC1" represents the projection of anionic ground-state wavefunction onto the neutral PES.

dynamical calculations as an indispensable tool for shedding light on polyatomic transition-state dynamics in complex chemical systems.

Methods

Experimental methods

In this study, we acquired the high-resolution binding energy spectra of $ClNH_3^-$ employing the cryogenic slow-electron velocity-map imaging (cryo-SEVI) method. Details of our cryo-SEVI apparatus can be found elsewhere[57]. Briefly, the $ClNH_3^-$ anions were generated by expanding trace amounts of CCl_4 with ammonia gas (~0.5 MPa) through a pulsed valve equipped with a high-voltage discharge ion source[58]. The nascent $ClNH_3^-$ anions were directed through a hexapole ion guide, then collected and cooled in a radio frequency (RF) ion trap mounted on the second stage of closed-cycle helium refrigerator, with a nominal temperature of 8 K. The trapped anions were cooled down to their ground vibrational states after sufficient collisions with a buffer gas (20% H_2 and 80% He) for 45 ms, and were subsequently ejected from the cold trap into an orthogonal Wiley-McLaren type time-of-flight (TOF) mass spectrometer[59]. The $^{35}ClNH_3^-$ anions were selectively filtered with a mass gate and intercepted by a detachment laser in the interaction region of velocity-map imaging (VMI)[60]. Photodetachment was performed at various photon energies with a tunable ultraviolet laser of an optical parametric oscillator (OPO, 210–405 nm, line width ~6 cm^{-1}) pumped by a Quanta-Ray Lab 190 Nd:YAG laser. The outgoing photoelectrons were projected onto a set of microchannel plates coupled with a phosphor screen and recorded using a charge-coupled device (CCD) camera. Energy calibration was carried out using the known spectra of $^{35}Cl^-$ at various photon energies. The projected 2D photoelectron image was used to reconstruct the 3D photoelectron distribution via the maximum entropy velocity Legendre reconstruction (MEVELER) method[61]. The cryo-SEVI features a high resolution for low-kinetic-energy photoelectrons, typically a few cm^{-1} near the photodetachment threshold[62]. A series of high-resolution spectra at different photon energies were concatenated to produce a full spectrum.

Computational Methods

The quantum dynamics calculations were performed to simulate the photodetachment process. The reactive system studied in this work is characterized by atom-tetra-atom (A-BCDE) Jacobi coordinates, as shown in Supplementary Fig. 1. The full-dimensional Hamiltonian of the system is expressed as ($\hbar$=1 hereafter)[63]:

$$\hat{H} = -\frac{1}{2\mu_R}\frac{\partial^2}{\partial R^2} - \frac{1}{2\mu_{r_1}}\frac{\partial^2}{\partial r_1^2} + \frac{\left(\hat{J}_{tot} - \hat{j}\right)^2}{2\mu_R R^2} + \frac{\hat{l}_1^2}{2\mu_1 r_1^2} + \frac{\hat{l}_2^2}{2\mu_2 r_2^2} + \frac{\hat{j}_3^2}{2\mu_3 r_3^2} + \hat{V}(R, r_1, r_2, r_3, \theta_1, \theta_2, \theta_3, \varphi_1, \varphi_2) \quad (1)$$

where R, r_1, r_2, and r_3 are defined as the distance between Cl_A and the center of mass (COM) of $H_BH_CH_DN_E$, the distance from H_B to the COM of $H_CH_DN_E$, the distance from H_C to the COM of H_DN_E, and the interatomic distance of H_DN_E, respectively, and the corresponding reduced masses are denoted by μ_R, μ_1, μ_2, and μ_3. J_{tot} is the total angular momentum of the system, which is set to zero in this calculation. j_3 is the rotational angular momentum of H_DN_E, l_2 is the orbital angular momentum of H_C with respect to H_DN_E, l_1 is orbital angular momentum of H_B with respect to $H_CH_DN_E$, and J is the coupled angular momentum of l_1, l_2 and j_3.

The photoelectron detachment process of an anion was described within the Condon approximation, which treats electron ejection as instantaneous relative to nuclear motion. Under this assumption, the photoelectron spectrum was represented by the Franck-Condon factor between the anionic wavefunction and neutral scattering (or bound state) wavefunction. In the simulations, the initial wave packet was prepared as the ground vibrational eigenstate of the anion, obtained by diagonalizing the nine-dimensional Hamiltonian on the anionic potential energy surface (PES). The initial wave packet is propagated on the neutral PES using the Chebyshev propagator. The energy spectrum was obtained through cosine Fourier transformation of the corresponding Chebyshev autocorrelation function. Additional details regarding the quantum dynamics methodology were provided in the Supplementary Computational Methods.

The neutral PES employed in the dynamics calculations was adopted from earlier work by some of the authors[48]. It was constructed by fitting approximately 52,000 ab initio energy points at the UCCSD(T)-F12a/aug-cc-pVTZ level of theory[64]. In this work, the anionic PES was newly constructed by fitting a total of 8794 energy points at the same level of theory. The energy range of the sampled data points spans approximately 12,000 cm^{-1} from the global minimum. The flexible, fundamental invariant-neural network method[65] was applied for the fitting, with the neural network architecture being 20-30-60-1, resulting in a root mean square error of 4.3 cm^{-1}.

Data availability

The raw spectral and calculated data of figures generated in this study have been provided in the figshare database and can be obtained at https://doi.org/10.6084/m9.figshare.31130017. The measured data of all peaks and the numerical parameters used in the calculation in this study are provided in the Supplementary Information.

Code availability

The associated codes, such as the subroutine to generate anion and neutral PESs and the quantum scattering code, are available on GitHub at https://github.com/apmtcc/A-BCDE and described in the README file.

References

1. Yuan, D. et al. Observation of the geometric phase effect in the H + HD → H_2 + D reaction. *Science* **362**, 1289–1293 (2018).
2. Chen, W. et al. Quantum interference between spin-orbit split partial waves in the F + HD → HF + D reaction. *Science* **371**, 936–940 (2021).
3. Ren, Z., Sun, Z., Zhang, D. & Yang, X. A review of dynamical resonances in A + BC chemical reactions. *Rep. Prog. Phys.* **80**, 026401 (2017).
4. Wang, Y. et al. Stereodynamical control of the H + HD → H_2 + D reaction through HD reagent alignment. *Science* **379**, 191–195 (2023).
5. Dantus, M., Rosker, M. J. & Zewail, A. H. Real-time femtosecond probing of "transition states" in chemical reactions. *J. Chem. Phys.* **87**, 2395–2397 (1987).
6. Mokhtari, A., Cong, P., Herek, J. L. & Zewail, A. H. Direct femtosecond mapping of trajectories in a chemical reaction. *Nature* **348**, 225–227 (1990).
7. Kraus, P. M., Zürch, M., Cushing, S. K., Neumark, D. M. & Leone, S. R. The ultrafast X-ray spectroscopic revolution in chemical dynamics. *Nat. Rev. Chem.* **2**, 82–94 (2018).
8. Bjork, B. J. et al. Direct frequency comb measurement of OD + CO → DOCO kinetics. *Science* **354**, 444–448 (2016).
9. Eyring, H. The activated complex in chemical reactions. *J. Chem. Phys.* **3**, 107–115 (1935).
10. Polanyi, J. C. & Zewail, A. H. Direct observation of the transition state. *Acc. Chem. Res.* **28**, 119–132 (1995).
11. Truhlar, D. G., Garrett, B. C. & Klippenstein, S. J. Current status of transition-state theory. *J. Phys. Chem.* **100**, 12771–12800 (1996).
12. Guo, H. & Liu, K. Control of chemical reactivity by transition-state and beyond. *Chem. Sci.* **7**, 3992–4003 (2016).
13. Zare, R. N. Laser control of chemical reactions. *Science* **279**, 1875–1879 (1998).

14. Metz, R. B., Weaver, A., Bradforth, S. E., Kitsopoulos, T. N. & Neumark, D. M. Probing the transition state with negative ion photodetachment: the chlorine atom + hydrogen chloride and bromine atom + hydrogen bromide reactions. *J. Phys. Chem.* **94**, 1377–1388 (1990).
15. DeVine, J. A. et al. Non-adiabatic effects on excited states of vinylidene observed with slow photoelectron velocity-map imaging. *J. Am. Chem. Soc.* **138**, 16417–16425 (2016).
16. DeVine, J. A. et al. Autodetachment from vibrationally excited vinylidene anions. *J. Phys. Chem. Lett.* **9**, 1058–1063 (2018).
17. DeVine, J. A. et al. Encoding of vinylidene isomerization in its anion photoelectron spectrum. *Science* **358**, 336–339 (2017).
18. Manolopoulos, D. E. et al. The Transition State of the F + H_2 Reaction. *Science* **262**, 1852–1855 (1993).
19. Weaver, A. & Neumark, D. M. Negative-ion photodetachment as a probe of bimolecular transition states: the F + H_2 reaction. *Faraday Discuss Chem. Soc.* **91**, 5–16 (1991).
20. Garand, E., Zhou, J., Manolopoulos, D. E., Alexander, M. H. & Neumark, D. M. Nonadiabatic interactions in the Cl + H_2 reaction probed by ClH_2^- and ClD_2^- photoelectron imaging. *Science* **319**, 72–75 (2008).
21. Yacovitch, T. I. et al. Vibrationally resolved transition state spectroscopy of the F + H_2 and F + CH_4 reactions. *Faraday Discuss* **157**, 399–414 (2012).
22. Cheng, M. et al. Communication: probing the entrance channels of the X + CH_4 → HX + CH_3 (X = F, Cl, Br, I) reactions via photodetachment of X^-–CH_4. *J. Chem. Phys.* **134**, 191102 (2011).
23. Babin, M. C. et al. Observation of resonances in the transition state region of the F + NH_3 reaction using anion photoelectron spectroscopy. *Nat. Chem.* **15**, 194–199 (2023).
24. Zhang, R., Yan, S., Song, H., Guo, H. & Ning, C. Probing the activated complex of the F + NH_3 reaction via a dipole-bound state. *Nat. Commun.* **15**, 3858 (2024).
25. Weichman, M. L. et al. Feshbach resonances in the exit channel of the F + CH_3OH → HF + CH_3O reaction observed using transition-state spectroscopy. *Nat. Chem.* **9**, 950–955 (2017).
26. Otto, R. et al. Imaging dynamics on the F + H_2O → HF + OH potential energy surfaces from wells to barriers. *Science* **343**, 396–399 (2014).
27. Zhang, X., Li, L., Chen, J., Liu, S. & Zhang, D. H. Feshbach resonances in the F + H_2O → HF + OH reaction. *Nat. Commun.* **11**, 223 (2020).
28. Xu, Z. F. & Lin, M. C. Computational studies on the kinetics and mechanisms for NH_3 reactions with ClO_x (x = 0–4) radicals. *J. Phys. Chem. A* **111**, 584–590 (2007).
29. Westenberg, A. A. & deHaas, N. Rates of H + CF_3Br and Cl + NH_3. *J. Chem. Phys.* **67**, 2388–2390 (1977).
30. Gao, Y. et al. Thermochemistry is not a lower bound to the activation energy of endothermic reactions: a kinetic study of the gas-phase reaction of atomic chlorine with ammonia. *J. Phys. Chem. A* **110**, 6844–6850 (2006).
31. Markovich, G., Cheshnovsky, O. & Kaldor, U. Charge transfer excitations in the photoelectron spectrum of Cl^-NH_3: Experiment and calculation. *J. Chem. Phys.* **99**, 6201–6204 (1993).
32. Moradi, C. P., Xie, C., Kaufmann, M., Guo, H. & Douberly, G. E. Two-center three-electron bonding in $ClNH_3$ revealed via helium droplet infrared laser Stark spectroscopy: entrance channel complex along the Cl + NH_3 → $ClNH_2$ + H reaction. *J. Chem. Phys.* **144**, 164301 (2016).
33. Kondo, S., Tokuhashi, K., Takahashi, A. & Kaise, M. Ab initio study of reactions between halogen atoms and various fuel molecules by Gaussian-2 theory. *J. Hazard Mater.* **79**, 77–86 (2000).
34. Monge-Palacios, M., Rangel, C., Corchado, J. C. & Espinosa-GarcÍA, J. Analytical potential energy surface for the reaction with intermediate complexes NH_3 + Cl → NH_2 + HCl: application to the kinetics study. *Int J. Quantum Chem.* **112**, 1887–1903 (2012).
35. Monge-Palacios, M. & Espinosa-Garcia, J. Reaction-path dynamics calculations of the Cl + NH_3 hydrogen abstraction reaction: the role of the intermediate complexes. *J. Phys. Chem. A* **114**, 4418–4426 (2010).
36. Skouteris, D. et al. van der Waals interactions in the Cl + HD reaction. *Science* **286**, 1713–1716 (1999).
37. Czakó, G. & Bowman, J. M. CH stretching excitation steers the F atom to the CD bond in the F + CHD_3 reaction. *J. Am. Chem. Soc.* **131**, 17534–17535 (2009).
38. Li, J., Jiang, B. & Guo, H. Enhancement of bimolecular reactivity by a pre-reaction van der Waals complex: the case of F + H_2O → HF + HO. *Chem. Sci.* **4**, 629–632 (2013).
39. Liu, K. Vibrational control of bimolecular reactions with methane by mode, bond, and stereo selectivity. *Annu Rev. Phys. Chem.* **67**, 91–111 (2016).
40. Czakó, G. & Bowman, J. M. Reaction dynamics of methane with F, O, Cl, and Br on ab initio potential energy surfaces. *J. Phys. Chem. A* **118**, 2839–2864 (2014).
41. Carrascosa, E., Meyer, J. & Wester, R. Imaging the dynamics of ion–molecule reactions. *Chem. Soc. Rev.* **46**, 7498–7516 (2017).
42. Fu, B., Shan, X., Zhang, D. H. & Clary, D. C. Recent advances in quantum scattering calculations on polyatomic bimolecular reactions. *Chem. Soc. Rev.* **46**, 7625–7649 (2017).
43. Xu, Y., Xiong, B., Chang, Y. C. & Ng, C.-Y. Quantum-vibrational-state-selected integral cross sections and product branching ratios for the ion-molecule reactions of $N_2^+(X^2\Sigma_g^+; v^+ = 0–2)$ + H_2O and $H_2O^+(X^2B_1: v_1^+v_2^+v_3^+ = 000$ and 100) + N_2 in the collision energy range of 0.04–10.00 eV. *Astrophys J.* **861**, 17 (2018).
44. Song, H. & Guo, H. Theoretical insights into the dynamics of gas-phase bimolecular reactions with submerged barriers. *ACS Phys. Chem. Au* **3**, 406–418 (2023).
45. Monge-Palacios, M., Corchado, J. C. & Espinosa-Garcia, J. Quasi-classical trajectory study of the role of vibrational and translational energy in the $Cl(^2P)$ + NH_3 reaction. *Phys. Chem. Chem. Phys.* **14**, 7497–7508 (2012).
46. Monge-Palacios, M., Yang, M. & Espinosa-García, J. QCT and QM calculations of the $Cl(^2P)$ + NH_3 reaction: influence of the reactant well on the dynamics. *Phys. Chem. Chem. Phys.* **14**, 4824–4834 (2012).
47. Tu, Z. et al. Accurate ab initio based potential energy surface and kinetics of the Cl + NH_3 → HCl + NH_2 reaction. *J. Chem. Phys.* **161**, 034304 (2024).
48. Chen, Y. et al. Revealing a heavy-atom assisted rotation mechanism in the H + NH_2Cl multi-channel reaction. *J. Phys. Chem. A* **129**, 2887–2895 (2025).
49. Hock, C., Kim, J. B., Weichman, M. L., Yacovitch, T. I. & Neumark, D. M. Slow photoelectron velocity-map imaging spectroscopy of cold negative ions. *J. Chem. Phys.* **137**, 244201 (2012).
50. Tang, R. et al. Candidate for laser cooling of a negative ion: high-resolution photoelectron imaging of Th^-. *Phys. Rev. Lett.* **123**, 203002 (2019).
51. Tang, R., Fu, X. & Ning, C. Accurate electron affinity of Ti and fine structures of its anions. *J. Chem. Phys.* **149**, 134304 (2018).
52. León, I., Yang, Z., Liu, H.-T. & Wang, L.-S. The design and construction of a high-resolution velocity-map imaging apparatus for photoelectron spectroscopy studies of size-selected clusters. *Rev. Sci. Instrum.* **85**, 083106 (2014).
53. Ning, C. & Lu, Y. Electron affinities of atoms and structures of atomic negative ions. *J. Phys. Chem. Ref. Data* **51**, 021502 (2022).
54. Yan, S., Lu, Y., Zhang, R. & Ning, C. Electron affinities in the periodic table and an example for as. *Chin. J. Chem. Phys.* **37**, 1–12 (2024).
55. van Bochove, M. A., Swart, M. & Bickelhaupt, F. M. Stepwise walden inversion in nucleophilic substitution at phosphorus. *Phys. Chem. Chem. Phys.* **11**, 259–267 (2009).

56. Sansonetti, J. E. & Martin, W. C. Handbook of basic atomic spectroscopic data. *J. Phys. Chem. Ref. Data* **34**, 1559–2259 (2005).
57. Tang, R. et al. Observation of electric-dipole transitions in the laser-cooling candidate Th^- and its application for cooling antiprotons. *Phys. Rev. A* **103**, 042817 (2021).
58. Yan, S., Zhang, R. & Ning, C. Precision measurement of the electron affinity of chlorine via high-resolution photoelectron spectroscopy. *J. Phys. Chem. Lett.* **15**, 7735–7739 (2024).
59. Wiley, W. C. & McLaren, I. H. Time-of-flight mass spectrometer with improved resolution. *Rev. Sci. Instrum.* **26**, 1150–1157 (1955).
60. Eppink, A. T. J. B. & Parker, D. H. Velocity map imaging of ions and electrons using electrostatic lenses: Application in photoelectron and photofragment ion imaging of molecular oxygen. *Rev. Sci. Instrum.* **68**, 3477–3484 (1997).
61. Dick, B. Inverting ion images without Abel inversion: maximum entropy reconstruction of velocity maps. *Phys. Chem. Chem. Phys.* **16**, 570–580 (2014).
62. Tang, R., Fu, X., Lu, Y. & Ning, C. Accurate electron affinity of Ga and fine structures of its anions. *J. Chem. Phys.* **152**, 114303 (2020).
63. Song, H., Zhu, Y., Pan, M. & Yang, M. Dissociative photodetachment of $H_3O_2^-$: a full-dimensional quantum dynamics study. *Phys. Chem. Chem. Phys.* **23**, 22298–22304 (2021).
64. Knizia, G., Adler, T. B. & Werner, H.-J. Simplified CCSD(T)-F12 methods: theory and benchmarks. *J. Chem. Phys.* **130**, 054104 (2009).
65. Shao, K., Chen, J., Zhao, Z. & Zhang, D. H. Communication: fitting potential energy surfaces with fundamental invariant neural network. *J. Chem. Phys.* **145**, 071101 (2016).

Acknowledgements

We thank the National Natural Science Foundation of China (NSFC) (Grant Nos. 12374244 and 12341401 to C.N., 22573116 to H.S.). S.Y. is supported by the National Science and Technology Major Project (Grant No. J2022-III-0007-0016) and the Director Foundation of Institute of Engineering Thermophysics, Chinese Academy of Sciences (Grant No. 555270101). This work is also supported by the Hubei Provincial Natural Science Foundation of China (Grant No. 2024AFA029).

Author contributions

The experiments were conceived by C.N. and carried out by S.Y., W.J., J.C., and R.Z. The data analysis was performed by S.Y. with support from C.N. The calculations were conceived by M.Y. and H.S. The paper was written by S.Y., H.S., and C.N.

Competing interests

The authors declare no competing interests.

Additional information

Supplementary information The online version contains supplementary material available at https://doi.org/10.1038/s41467-026-71634-2.

Correspondence and requests for materials should be addressed to Hongwei Song or Chuangang Ning.

Peer review information : *Nature Communications* thanks the anonymous reviewers for their contribution to the peer review of this work. A peer review file is available.